Ground deformation in the Taupo Volcanic Zone, New Zealand, observed by ALOS PALSAR interferometry

Sergey Samsonov,[1,2] John Beavan,[1] Pablo J. González,[3] Kristy Tiampo[3] and José Fernández[4,5]

[1]*GNS Science, Lower Hutt, New Zealand. E-mail: ssamson@uwo.ca*
[2]*European Center for Geodynamics and Seismology, Walferdange, Grand-Duchy of Luxembourg*
[3]*Department of Earth Sciences, University of Western Ontario, London, Ontario, Canada*
[4]*Instituto de Astronomia y Geodesia (CSIC-UCM), Fac. C. Matematicas, Madrid, Spain*
[5]*Now at Instituto de Geociencias (CSIC-UCM), Fac. C. Matematicas, Madrid, Spain*

GJI Gravity, geodesy and tides

SUMMARY

We present ground deformation measurements in the Taupo Volcanic Zone (TVZ) using differential interferomeric synthetic aperture radar (DInSAR) observations collected by ALOS PALSAR during 2006–2010, and compare them with displacement observations from continuous GPS. We acquired and processed DInSAR images from two ascending paths (324 and 325) and one descending path (628) covering the TVZ, and produced linear deformation rates and time series of deformation. The DInSAR results were improved by using a modified version of the small baseline subset (SBAS) algorithm that simultaneously solves for deformation rates and residual topographic noise. The accuracy of the DInSAR displacement rates along line-of-sight to the satellite is 0.5–2 cm yr^{-1} depending on the number of SAR images and their coherence. We found good agreement between the DInSAR-derived displacement rates and those measured by continuous GPS for the two ascending paths (correlation 0.94 ± 0.01 and 0.89 ± 0.02); the DInSAR uncertainties were too large to make a useful comparison for the descending path (correlation 0.66 ± 0.03). We identified ground deformation due to groundwater and steam extraction for geothermal power. To demonstrate the geophysical application, we modelled the deformation results using simplified sources for some of the geothermal signals using ellipsoidal and tabular approximations.

Key words: Time series analysis; Image processing; Satellite geodesy; Radar interferometry; Back-arc basin processes; New Zealand.

1 INTRODUCTION

Time series techniques have been used over the past 5–10 yr to derive ground deformation rates from sequences of DInSAR images (Ferretti *et al.* 2000; Lanari *et al.* 2004a; Burgmann *et al.* 2006; Kwoun *et al.* 2006). The technique has been particularly effective in relatively arid regions using C-band (∼5 cm wavelength) interferometry (Lanari *et al.* 2004a; Samsonov *et al.* 2010). In regions with dense vegetation, time series techniques using C-band have been unsuccessful because of loss of coherence between subsequent images (e.g. Hole *et al.* 2007). In vegetated regions, radar images from the L-band PALSAR sensor on the ALOS satellite (Rosenqvist *et al.* 2007) show much higher coherence than C-band images (Samsonov 2010). Here, we use ALOS data from the Taupo Volcanic Zone (TVZ) to investigate how well L-band DInSAR time series techniques work in this environment, which includes large tracts of farmland and forestry, for both short wavelength signals due to geothermal groundwater extraction and longer wavelength signals of tectonic and volcanic origin.

The TVZ (Fig. 1) is a volcanic arc located in the central North Island, New Zealand, with dimensions 300 × 60 km aligned SW to NE. It is a backarc rifting region associated with subduction of the Pacific tectonic plate beneath the Australian Plate. Ground deformation signals expected in the region include a NW–SE tectonic extension of 8–15 mm yr^{-1} over a width of 20–30 km (Darby *et al.* 2000; Wallace *et al.* 2004) and a number of more compact deformation sources associated with groundwater and steam extraction for geothermal power production. Ground deformation from the latter sources may have rates of tens of millimetres per year over lateral dimensions of several kilometres (e.g. Allis 2000; Allis *et al.* 2009; Bromley *et al.* 2009). Ground deformation signals of volcanic origin, or due to volcano–tectonic interaction, are also present in the region (e.g. Peltier *et al.* 2009) but little is known about the dimensions or magnitudes of such sources. L-band interferometry is likely to be an important source of information on such signals, if the technique can be demonstrated to have sufficiently low noise characteristics.

In this paper, we present deformation maps calculated from ALOS PALSAR images acquired over a ∼3-yr period between
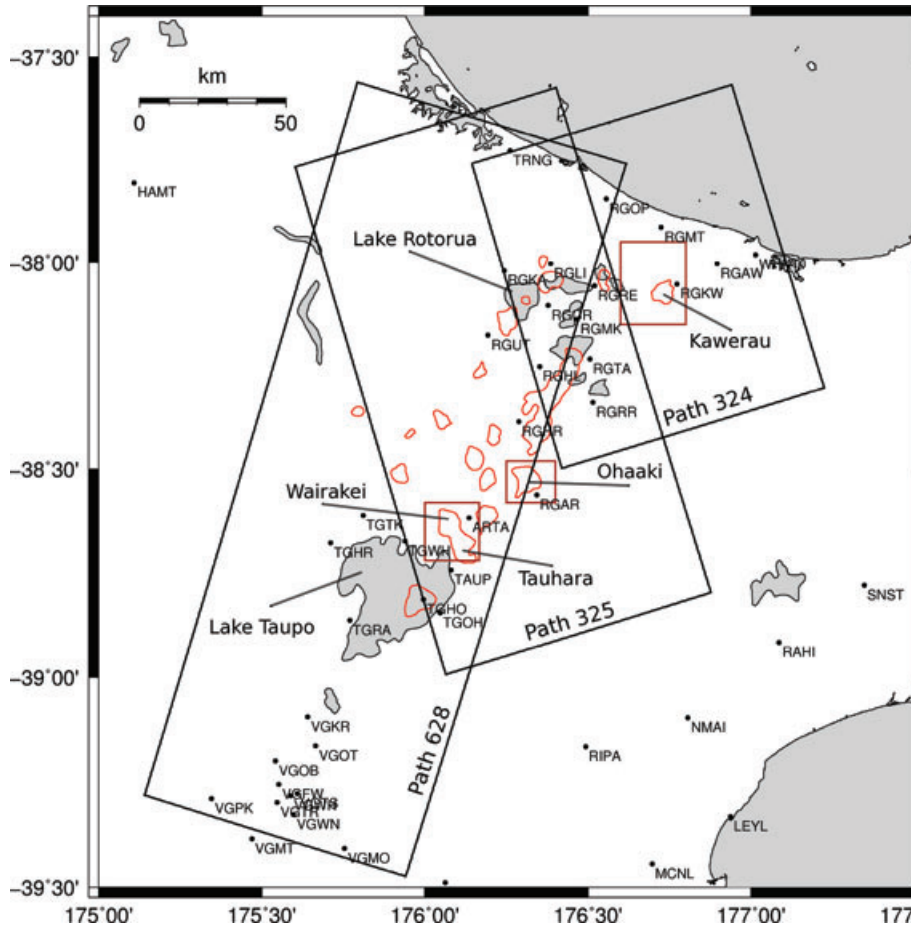
Figure 1. Location map showing Taupo Volcanic Zone and footprints of ALOS images used in this study (ascending paths 324–325 and descending path 628). Geothermal fields are outlined in red (modified from Bibby *et al.* 1995; Hole *et al.* 2007).

2006 December and 2010 January. We utilize data from two ascending paths, 324 (one frame) and 325 (two frames), and from descending path 628 (four frames). A standard methodology for stacking DInSAR scenes has been shown to be of limited use for ALOS PALSAR data (Samsonov *et al.* 2008) and an advanced technique has been developed to produce displacement rates and time series with higher accuracy (Samsonov 2010; Samsonov *et al.* 2011). To validate the accuracy of the DInSAR displacement rates we compare them with displacement rates estimated from about 30 continuous GPS (cGPS) sites (www.geonet.org.nz) located within the DInSAR images. Due to the ∼24 cm wavelength of ALOS PALSAR the measurement accuracy is in most cases of about the same magnitude as the expected ground deformation signal (1–2 cm yr^{-1}). We therefore generally present only a qualitative interpretation. However, for some of the short wavelength and high amplitude geothermal signals we model the data using simple techniques. In this modelling, our purpose is not to discover new information about the deformation sources, which are generally already well characterized by terrestrial measurements, but to demonstrate that the DInSAR time series results can be modelled with plausible if simplified models. If this is the case, future measurements using longer and more accurate DInSAR time series can be expected to usefully augment existing terrestrial data, or to provide unique observations in regions where terrestrial data do not exist.

2 TECTONIC, VOLCANIC AND GEOTHERMAL BACKGROUND

Based on the type of volcanism, the TVZ is divided into three segments (Wilson *et al.* 1995). The northeast and southwest segments contain andesitic to dacitic composite volcanoes and the central segment is defined by rhyolitic volcanism that has produced over 10 000–20 000 km^3 of material from a few large caldera systems. A study utilizing ^{40}Ar/^{39}Ar dating suggests that major caldera forming events in the TVZ were not evenly distributed in space and time but clustered in three periods of more intense activity separated by significant gaps in time or changes in source position (Houghton *et al.* 1995). The earliest eruption (Period I: 1.68–1.53 Ma) at Mangakino volcanic centre located on the west margin of the zone (Fig. 1) was followed by an eruption at Kapenga volcanic centre (Period II: 0.77–0.68 Ma) and later by eruptions at the remaining volcanic centres (Period III: 0.34 Ma–present). The two most recent volcanic centres, Taupo and Okataina, remain highly active to the present day.

Conductive heat transport between the ductile base of the crust at ∼16 km (Stratford & Stern 2004) and the bottom of the brittle convective region at ∼8 km (Bibby *et al.* 1995), where the hydrothermal convection originates, can supply only 60 per cent of the observed heat flow at the surface. It was suggested by Bibby *et al.* (1995) that repeated intrusions from the mantle are the probable cause of the

remaining 40 per cent of the heat transfer. Stress redistribution associated with such intrusions of ductile material at depth is likely to lead to large temporal and spatial variations in surface deformation rates. A late Quaternary NW–SE oriented extension in the TVZ has been estimated from fault slip data to be in the range of 0.12–0.28 cm yr^{-1} at the surface and 0.36–1.02 cm yr^{-1} at seismogenic depths of 6–10 km (Villamor & Berryman 2001). Recent geodetic studies of Darby *et al.* (2000) and Wallace *et al.* (2004) suggest current NW–SE oriented extension at close to 1 cm yr^{-1} just north of Lake Taupo and *ca.* 1.2–1.5 cm yr^{-1} along the Bay of Plenty (BoP) coast; however, this extension is not uniform in space and time. The hydrothermal activity caused by the large heat flow at twenty-three geothermal systems in the TVZ (Fig. 1), clearly defined by the electrical resistivity studies reported in Stagpoole & Bibby (1998), has been intensively exploited for power generation and heating since the 1950s. Groundwater withdrawal without proper recharge has produced localized ground subsidence with a maximum magnitude of ~15 m at Wairakei geothermal field Allis (2000).

The extent and rate of subsidence at producing geothermal centres in the TVZ is monitored by precise levelling across networks of benchmarks repeated at intervals of 1–5 yrs (Allis 2000; Allis *et al.* 2009). Such monitoring is important to provide a constraint on the permeability and compressibility properties of the compacting formations as well as to monitor potential damage to infrastructure.

3 DATA AND METHODOLOGY

3.1 DInSAR

Differential synthetic aperture radar interferometry (DInSAR) is a remote sensing technique that measures ground deformation with high spatial resolution and accuracy over a large area (Massonnet & Feigl 1998; Rosen *et al.* 2000). An interferogram is calculated from two SAR images (called master and slave) acquired at two distinct times by performing the following processing steps: coarse and then fine image co-registration, slave to master re-sampling, interferogram formation, removal of earth curvature and topographic components, filtering and finally phase unwrapping. Additional and somewhat subjective processing steps such as orbital correction (e.g. removal of linear or quadratic trend) and phase interpolation over incoherent regions may also be performed to increase the quality and the coverage of the interferogram. After this processing the differential interferogram reveals the component of ground deformation that occurred between the two observations along the line-of-sight (LOS) between the ground and the satellite.

One of the largest limitations of conventional DInSAR is signal decorrelation caused by diffusive scattering from vegetation. The decorrelation is particularly significant for short wavelength sensors, such as X- and C-band, and moderate for longer wavelength sensors such as the L-band ALOS PALSAR used in this study. Previous DInSAR results in the TVZ using C-band data from the ERS-2 and ENVISAT satellites for the 1996–2005 period revealed ground subsidence at Tauhara-Wairakei, Ohaaki and Rotorua geothermal fields (Hole *et al.* 2007). On a larger spatial scale C-band interferometry produced limited results due to severe decorrelation effects.

For this study, we use L-band ALOS PALSAR data with ground resolution of ~50 m and spatial coverage of 70 × 70 km from two ascending and one descending paths (Table 1). We use: (1) 13 images spanning 2006 December 26–2009 November 19 from ascending path 324 (frame 6410) that covers the northern part of the TVZ and BoP in a NW–SE direction; (2) 15 images (30 frames in

Table 1. ALOS PALSAR images used in this study (in YYYYMMDD format).

628 (dsc)	324 (asc)	325 (asc)
20070715	20061227	20070113
20070830	20070211	20070228
20080301	20070814	20070716
20080416	20071230	20070831
20080601	20080214	20071016
20080717	20080331	20071201
20080901	20081001	20080116
20081202	20090101	20080302
20090117	20090216	20080417
20090604	20090704	20080902
20090904	20090819	20081018
20091205	20091004	20090118
	20091119	20090721
		20091021
		20100121

total) spanning 2007 January 13–2010 January 21 from ascending path 325 (frames 6390–6410) that covers the central TVZ in a NW–SE direction; and (3) 12 images (48 frames in total) spanning 2007 July 15–2009 December 5 from descending path 628 (frames 4390–4420) that covers most of the TVZ in a SW–NE direction. We used both fine beam single and fine beam dual polarization data.

All data were acquired in ALOS-specific raw L1.0 format and processed to single look complex format with GAMMA software (Wegmuller & Werner 1997). Two frames from ascending path 325 and four frames from descending path 628 were concatenated in one strip each and processed simultaneously. The maximum magnitude of perpendicular baselines was set to 1200 m for descending pairs and 1000 m and 1400 m for ascending pairs from paths 324 and 325, respectively, and all possible differential interferograms satisfying these baseline criteria were generated. In total we obtained 19 interferograms for descending path 628, and 27 and 47 interferograms, respectively for ascending paths 324 and 325. The topographic component was removed using synthetic phase generated from the 50 m resolution Land Information New Zealand (LINZ) digital elevation model (DEM).

An orbit refinement was performed that attempted to remove orbital ramps from each differential interferogram. This algorithm extracts interferometric phase measurements for a number of highly coherent points within each interferogram and then solves for corrected baseline parameters using extracted phases and known topographic heights. The interferogram is then recalculated using corrected orbital parameters. The algorithm is able to successfully correct linear and quadratic orbital ramps, especially in the case of large perpendicular baselines and absence of long wavelength atmospheric errors. In case of severe atmospheric noise the algorithm is less accurate since it is not able to differentiate orbital and atmospheric components in the observed signal.

To extend spatial coverage to partially incoherent regions spatial interpolation was performed over a 16-pixel radius for each pixel with at least 16 valid pixels in its neighbourhood (equal to about 8 per cent). The interpolation step is very important for further small baseline subset (SBAS) processing since it is applied only to those pixels that are available on all interferograms.

Initially the standard stacking (Sandwell & Price 1998) and SBAS (Berardino *et al.* 2002; Usai 2003; Lanari *et al.* 2004b) algorithms were applied to produce average displacement rates and time series of deformation; however, these results were noisy. The largest

component of the noise was explained by the particular orbital pattern of the ALOS satellite. For ALOS during 2006–2010 the perpendicular baseline increases approximately linearly to 2.5–3 km over a period of several years and then resets to a negative 2.5–3 km. Using standard processing, which assumes the perpendicular baseline to vary randomly from image to image, this causes large apparent ground deformation signals correlated with topography and land usage. Samsonov (Samsonov 2010) developed a technique to attenuate the noise signal in SBAS processing by utilizing the known baseline vs. time correlation, and we use this in the present paper.

The time series were reconstructed by integration from calculated deformation rates (e.g. Kwoun *et al.* 2006) and finally linear displacement rates with corresponding errors were calculated by applying linear regression to the time series (e.g. Press *et al.* 2007).

3.2 Continuous GPS

A network of about 30 continuous GPS (cGPS) sites has been installed in the TVZ since 2006 to monitor 3-D ground deformation. A number of GPS campaigns have been conducted recently in the TVZ in addition to those used by Beavan & Haines (2001) and Wallace *et al.* (2004). However, the results from the campaigns are not used here as their vertical rates are much less accurate than those from cGPS especially if taken only over the 2006–2010 period of the DInSAR observations.

To assess the accuracy of the DInSAR measurements, we compare ground deformation observations from cGPS and DInSAR. We analyse the cGPS data with Bernese v5.0 software (Dach *et al.* 2007) holding IGS final orbits and earth orientation parameters fixed. We use relative, rather than absolute, antenna phase patterns. We incorporate ocean load estimates from Topex model 7.1 as calculated by Onsala Space Observatory (http://www.oso.chalmers.se/~loading/). The tropospheric zenith delay is estimated hourly and tropospheric tilt estimated daily, using Niell (1996) mapping functions. Ambiguities are fixed as far as possible using the Bernese software's quasi-ionosphere-free (QIF) strategy and the global ionosphere model produced daily by the Centre for Orbit Determination in Europe. Daily solutions are transformed to the ITRF2000/IGb00 reference frame using a 3-parameter Helmert transformation onto a set of regional (Australia and Pacific) IGS stations. For a GPS network of the spatial extent being analysed here, there is no significant advantage to using more recent ITRF2005/IGS05 orbits or to using absolute antenna phase patterns. The resulting daily-coordinate time series are regionally filtered (Wdowinski *et al.* 1997; Beavan 2005) using a set of New Zealand stations that have close to linear behaviour over the 2002–2010 time period. The velocities of the sites are estimated by linear regression on the resulting east, north and up component time series. We transform the horizontal velocities to a reference frame defined by sites in the north and west of the North Island well away from the TVZ and the plate boundary (KTIA, WHNG, AUCK, CORM, HAMT, MAHO, NPLY; see http://www.geonet.org.nz/resources/network/netmap.html). We use this, which is within ~1 mm yr⁻¹ of an Australian Plate reference frame (Beavan *et al.* 2002; Wallace *et al.* 2004), because we assume this region to be stable in our DInSAR processing. We add a constant to the vertical velocities so that the mean vertical velocity of the reference set is equal to zero.

In comparing the 3-D GPS displacement rates with the LOS rates derived from InSAR, we resolve the GPS rates along the line

of sight to the satellite by taking the dot product of the 3-D GPS rate with a unit vector along the LOS using precise directional cosines. The uncertainties in the GPS LOS rates are dominated by the uncertainty in the GPS vertical component, which is typically several times larger than the uncertainty in either of the horizontal components.

4 DINSAR RESULTS

We report here the LOS displacement rates derived from DInSAR time series processing for geothermal fields Kawerau, from path 324; Ohaaki, from path 325; and Tauhara-Wairakei, from paths 325 and 628 (see Fig. 1 for location). In the event that the true ground displacement is predominantly subsidence, this should show as a similar magnitude of LOS lengthening for both ascending and descending paths. Any northward component of horizontal ground displacement should also show as an identical signal in both ascending and descending images. Eastward ground motion should show as LOS lengthening for ascending paths and as a similar magnitude of LOS shortening for descending paths.

Linear displacement rates with corresponding errors for ascending paths 324, 325 are presented in Figs 2–3 and for descending path 628 are presented in the Supporting Information. The 70×70 km image from path 324 covers the northern TVZ and the BoP. LOS lengthening in this image is observed at the Kawerau geothermal field with rates close to 2–3 cm yr⁻¹ and also at Okataina volcanic centre with rates 1–2 cm yr⁻¹. The LOS lengthening at Kawerau geothermal field is localized, about 2–5 km in diameter, and at this location is likely to be largely due to ground subsidence. The LOS lengthening at Okataina covers a larger area, about 10–20 km in diameter, and we assume this signal to be of volcanic origin. The 70×140 km image from path 325 is located to the west of the path 324 image described previously. Localized subsidence is clearly observed at Ohaaki geothermal field and at Tauhara-Wairakei geothermal system, with rates 3 and 5–6 cm yr⁻¹, respectively. A few other regions of subsidence are visible but their cause is unknown. The 70×200 descending image from path 628 consists of four regular frames and covers the TVZ in the SW–NE direction. The area is characterized by generally low LOS rates with a number of regions of moderate (less than ~1 cm yr⁻¹) LOS lengthening. Rapid LOS lengthening with rates 5–6 cm yr⁻¹ is observed at Tauhara-Wairakei geothermal system. The uncertainties (up to 2 cm yr⁻¹ at 1σ) on the DInSAR rates are so large as to preclude a meaningful comparison with the cGPS rates. The large uncertainties are mainly due to lower coherence along this path (because of large perpendicular baselines), but also to a smaller number of images.

In Fig. 4 we compare, for all cGPS sites within the DInSAR image, displacement rates calculated by DInSAR with those derived from cGPS converted to line-of-sight by measurement their correlation coefficient. The 1σ uncertainty of these DInSAR measurements is approximately 0.5–1 cm yr⁻¹ while that of the cGPS rates is typically 0.1–0.3 cm yr⁻¹. The observed correlation between DInSAR and GPS is 0.94 ± 0.01, 0.89 ± 0.02 and 0.66 ± 0.03 for paths 324, 325 and 628 correspondingly.

The time series and spatial extent of cumulative ground deformation at Kawerau, Ohaaki and Tauhara-Wairakei geothermal systems are shown in Figs 5–8 with scales adjusted to capture the whole signal. A 1-D plot of deformation is also shown in Fig. 9 for the smaller subregions of fastest motion. This reveals a near constant subsidence rate at all geothermal fields with the rates mentioned above.
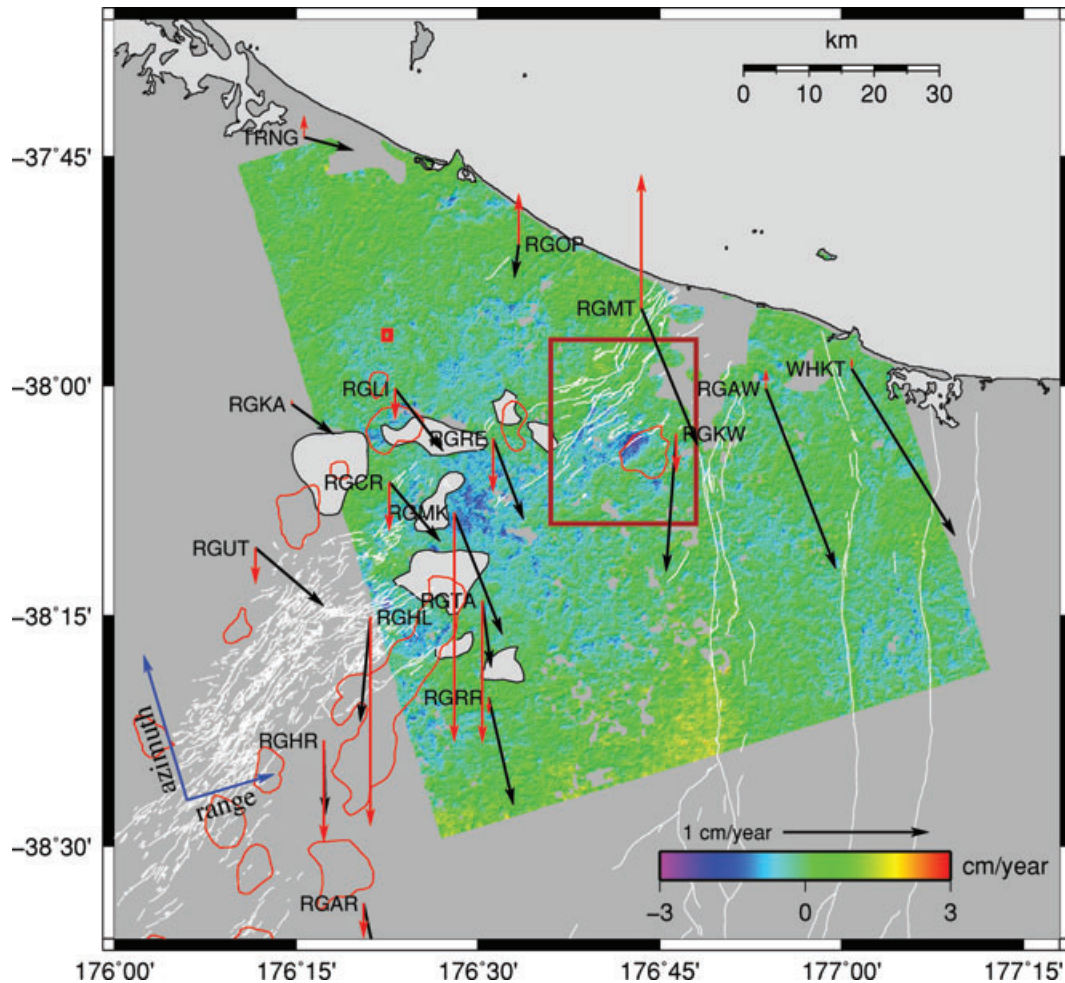
Figure 2. Line-of-sight displacement rates calculated by fitting linear trend to time series for ALOS PALSAR ascending path 324. cGPS vertical velocities relative to stable parts of New Zealand well away from the TVZ and the Hikurangi subduction interface are shown with red arrows. cGPS horizontal velocities relative to northwestern New Zealand (which is within ~1 mm yr^{-1} of an Australia-fixed reference frame) are shown with black arrows. Velocity uncertainties are not plotted but are typically 1 mm yr^{-1} for the horizontal and 2 mm yr^{-1} for the vertical. Brown rectangle outlines subsidence at Kawerau geothermal field. Red square shows reference region used in SBAS processing. Azimuth is the flight direction of the satellite and range is the look direction of the radar beam. Active faults are plotted in white (from GNS database).

In Fig. 10, we plot the DInSAR, SBAS and cGPS time series for a few cGPS sites. We think that moderate discrepancies at some sites (e.g. TAUP-325 and RGHL-628 as observed in Figs 4b and c) are most likely due to the small number of points and the high noise level in the DInSAR time series. If the true rates are reasonably constant, then additional images that extend the length of the time series will improve the accuracy of DInSAR displacement rate estimates.

In Fig. 11, we demonstrate topographic errors estimated by our modified SBAS algorithm that are present in two Digital Elevation Models available to us, the 90 m SRTM DEM and the 40 m LINZ (Land Information New Zealand) DEM. The magnitude of topographic errors ranges from −30 to 30 m on both DEMs, with standard deviation of 8.2 m and 8.7 m, respectively.

In Fig. 12 we shows examples of interferograms from path 628 affected by linear and quadratic orbital errors. Such orbital signal is clearly identifiable and is easy to remove by performing orbital refinement or by fitting a quadratic surface. However, it is impossible without prior knowledge to isolate the long wavelength deformation component (such as an extension) that also gets removed during orbital correction.

5 DISCUSSION

Our aim in this work is to investigate the feasibility and accuracy of L-band DInSAR for mapping ground deformation in a well-vegetated region, specifically the TVZ, New Zealand. The ALOS PALSAR sensor operates in the L-band with a wavelength of about 23.6 cm. In the case of good interferometric coherence and absence of atmospheric noise the accuracy of a single differential interferogram is proportional to the satellite wavelength, which for ALOS PALSAR is about four times worse than the accuracy of the commonly used C-band sensors, such as ERS-1/2 or ENVISAT. At the same time, sensitivity to ionospheric perturbations for L-band sensors is about sixteen times larger than for C-band sensors (Rignot 2000; Meyer *et al.* 2006). This sensitivity to ionospheric noise and the ability to produce coherent interferograms for pairs with large spatial baselines (causing large residual topographic noise) adds additional noise to the L-band DInSAR measurements that may be correlated over large regions. In the next subsections, we discuss the effects these noise sources have on our results and the processing methodology we use.
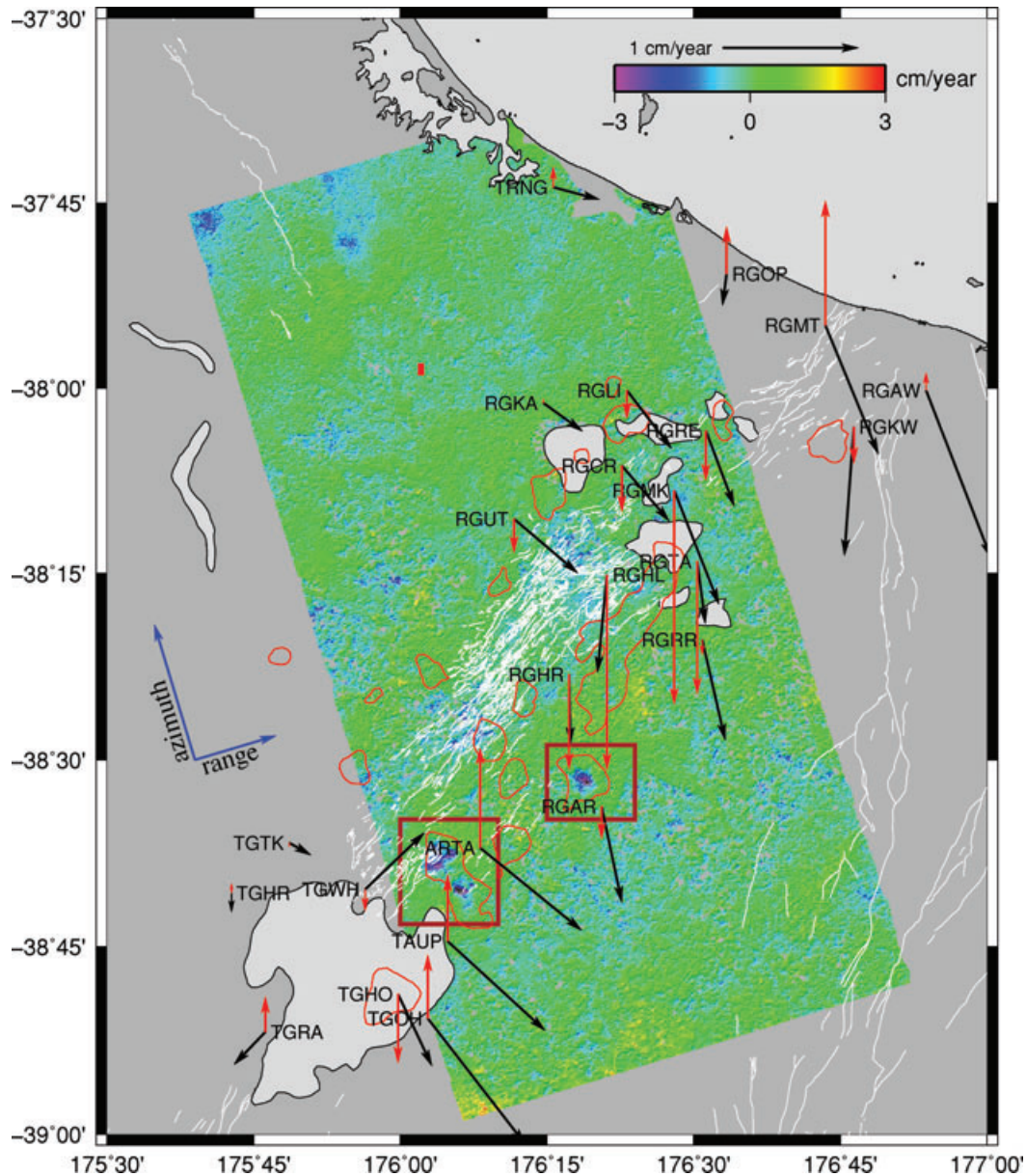
Figure 3. Line-of-sight displacement rates calculated by fitting linear trend to time series for ALOS PALSAR ascending path 325. cGPS velocities are plotted as described in Fig. 2. Red square shows reference region used in SBAS processing. Brown rectangles outline subsidence at Ohaaki (top panel) and Tauhara-Wairakei (bottom panel) geothermal systems.

5.1 Residual topographic noise

We observed that for the SRTM and LINZ DEMs the residual topographic noise in individual interferograms was significant, with a maximum magnitude close to 30 m (Fig. 11). The residual topographic noise was also spatially correlated, with a large spatial extent, often resembling the shapes of agricultural fields, forested areas, etc. Due to the particular non-random variation of the ALOS perpendicular baselines over time the residual topographic noise in the set of calculated interferograms is also temporally not random; therefore, it is not minimized during standard stacking or SBAS processing. The modified SBAS technique (Samsonov 2010; Samsonov *et al.* 2011) that simultaneously solves for deformation rates and residual topographic noise solves this problem, and significantly improves the accuracy of our results. The nature of the residual topographic noise is not clear at this time and needs to be

studied further. We believe that at least partially the residual topographic noise is caused by changes in land cover that occurred after the DEM was generated, and also by variations in vegetation and soil parameters (e.g. density, moisture level) that affect the interaction of the L-band SAR with reflective media.

5.2 Atmospheric and orbital noise

Tropospheric and ionospheric noise was observed on many interferograms. Localized effects caused by non-uniform distribution of water vapour in the troposphere did not cause any particular problem for the processing due to their limited extent and the relatively large number of images used. Such tropospheric signal in interferograms is easy to identify by comparing interferograms spanning a similar time period but having different master or slave images.
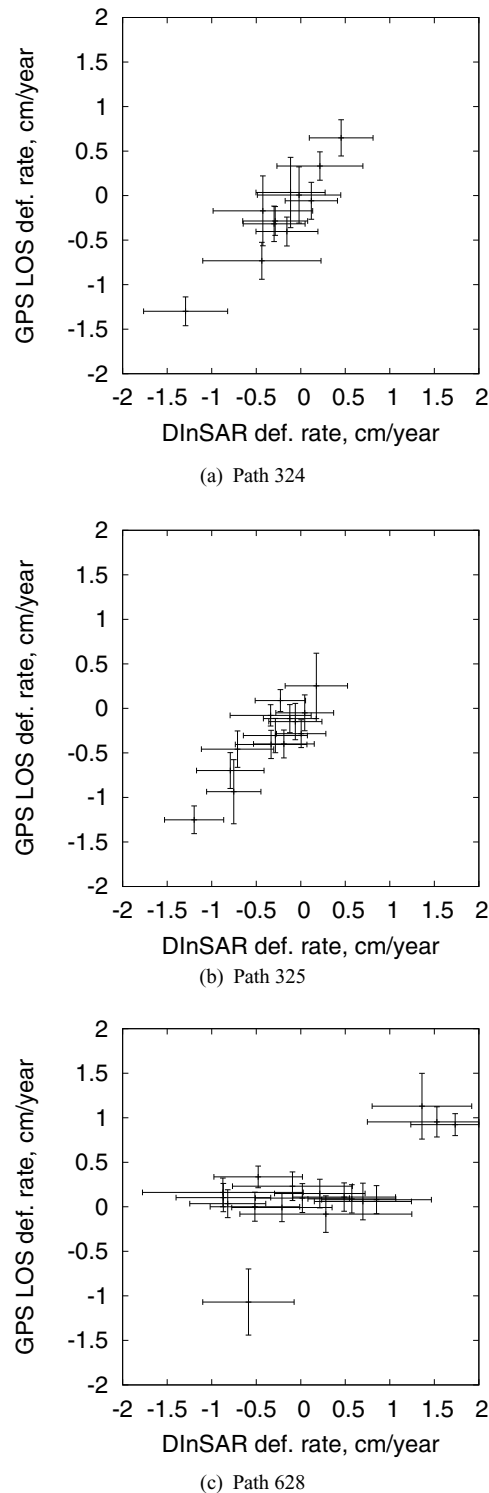
(a) Path 324

(b) Path 325

(c) Path 628

Figure 4. Comparison of cGPS velocities projected on line-of-sight and differential InSAR line-of-sight displacement rate measurements. Correlation coefficients between GPS and DInSAR are 0.94 ± 0.01, 0.89 ± 0.02 and 0.66 ± 0.03 for paths 324, 325 and 628 correspondingly. Error bars show $\pm 1\sigma$ uncertainties.

Medium to long wavelength (in comparison to image size) signals produced by ionospheric disturbances were harder to remove due to their interference with orbital and deformation components of the signal

Linear and quadratic trends were observed in approximately 50 per cent of the interferograms. Such ramps can be produced either by incorrect estimation of orbital parameters or by variations in TEC with a spatial wavelength much larger than the SAR image size. Such signals are usually easy to correct by fitting a linear or quadratic trends to the interferogram, or by performing baseline parameter refinement using interferometric phase and topographic heights for a number of highly coherent points within each interferogram as described earlier. In interferograms from descending path 628 that consists of four frames concatenated together we observed a large, well-defined quadratic trend in the azimuth direction. We found that application of high-pass filtering to individual interferograms successfully removes this signal; however, it also removes any long wavelength deformation component. In Fig. 12, it can be seen that even significant orbital ramps can be successfully removed.

In the case of the TVZ, orbit refinement should take into account the tectonic extension in a NW–SE direction across the TVZ and the rotation of the land east of the TVZ away from the western North Island (e.g. Wallace *et al.* 2004). This extension and rotation should show as an approximately linear trend across the deforming regions in the observed interferograms particularly on the descending orbit. However, the rates of tectonic motion are 1–1.5 cm yr^{-1}, corresponding to only about 25 per cent of a fringe over the 3-yr period of our images, which is below the noise level of our current data. We therefore ignore this tectonic extension and rotation in our current processing but recognize that it will have to be treated correctly when longer time series with lower noise levels are collected.

6 GEOTHERMAL SOURCE PARAMETERS FROM DINSAR MEASUREMENTS

Here, we attempt to estimate source parameters such as the annual rate of fluid volume change in the geothermal source regions using ascending and descending deformation maps provided in Figs 5–8. We do this to demonstrate that these short wavelength features can be sensibly modelled, which implies that L-band DInSAR data will be useful for interpreting similar signals in other regions with challenging environments. On the basis of previous knowledge of the overall location and subsurface features of the geothermal sites, we assume that the causative sources of ground deformation are mainly due to extraction of fluids from relatively shallow bodies (Allis 2000; Allis *et al.* 2009). We suppose that depending on their shape these bodies can be approximated by either an ellipsoid or a tabular source. The medium is considered to be a uniform, homogeneous and isotropic elastic half space, so we neglect any potential heterogeneity, such as medium layering. Medium layering often tends to enhance ground deformation, according to the elastic parameters of each horizon in the assumed Earth model (e.g. Hooper *et al.* 2002; Manconi *et al.* 2007). The elastic shear modulus (μ) and Poisson ratio (ν) were assumed to be 10 GPa and 0.25, respectively. At very shallow depths, the rigidity of crustal rocks is frequently lower than commonly assumed elastic properties for the lithosphere ($\mu = 30$–35 GPa) due to a higher percentage of voids, cracks and fluids, and the presence of soft sedimentary layers.

6.1 Ellipsoidal sources

For Kawerau, Ohaaki and Tauhara geothermal fields we assumed, based on the shape of the observed ground deformation, that the
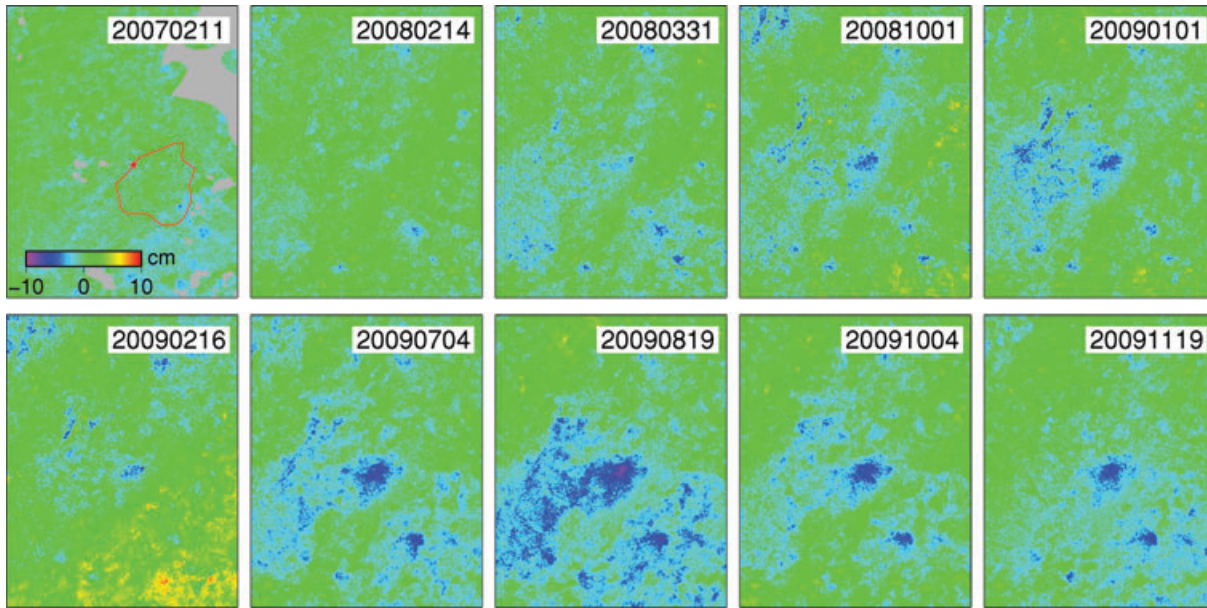
Figure 5. Time series of line-of-sight displacement at Kawerau geothermal field from ALOS PALSAR ascending path 324 starting from 20061227 (date in YYYYMMDD format). Coordinates of top-left hand side (TL) and bottom-right hand side (BR) corners are (−37.95N, 176.60E) and (−38.15N, 176.80E). Red star shows region of fastest subsidence.
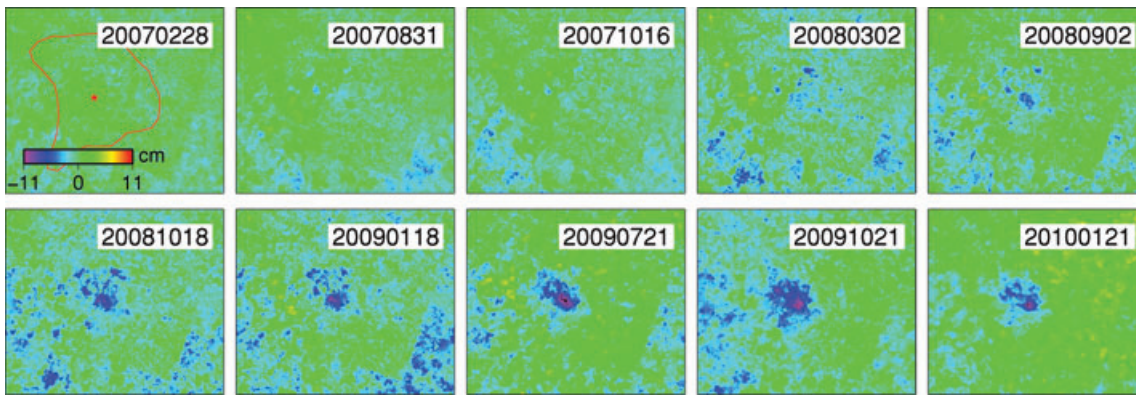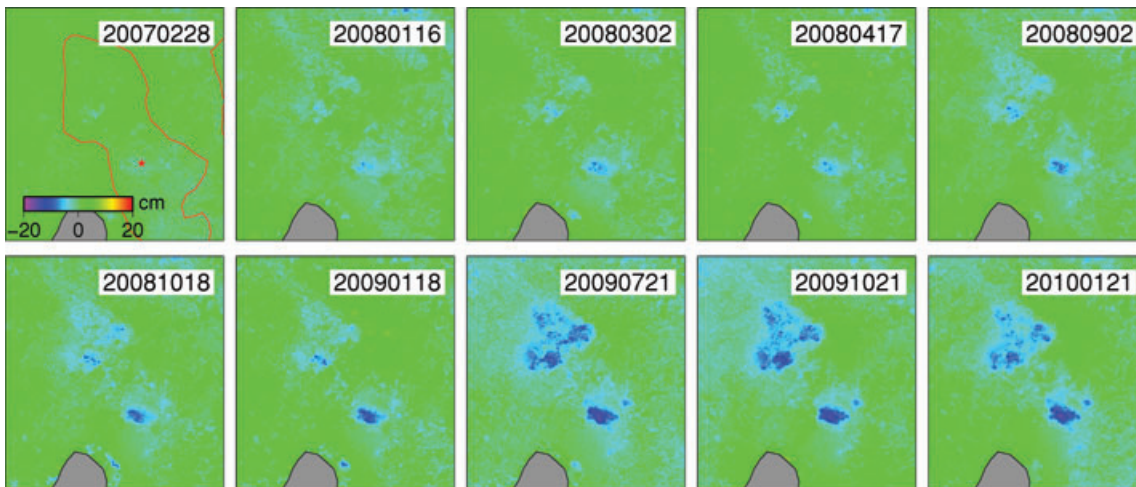

Figure 6. Time series of line-of-sight displacement at Ohaaki geothermal field from ALOS PALSAR ascending path 325 starting from 20070113 (date in YYYYMMDD format). Coordinates of TL and BR corners are (−38.48N, 176.25E) and (−38.58N, 176.40E). Red star shows region of fastest subsidence.

Figure 7. Time series of line-of-sight displacement at Tauhara-Wairakei geothermal system from ALOS PALSAR ascending path 325 starting from 20070113 (date in YYYYMMDD format). Coordinates of TL and BR corners are (−38.58N, 176.00E) and (−38.72N, 176.17E). Red star shows region of fastest subsidence.

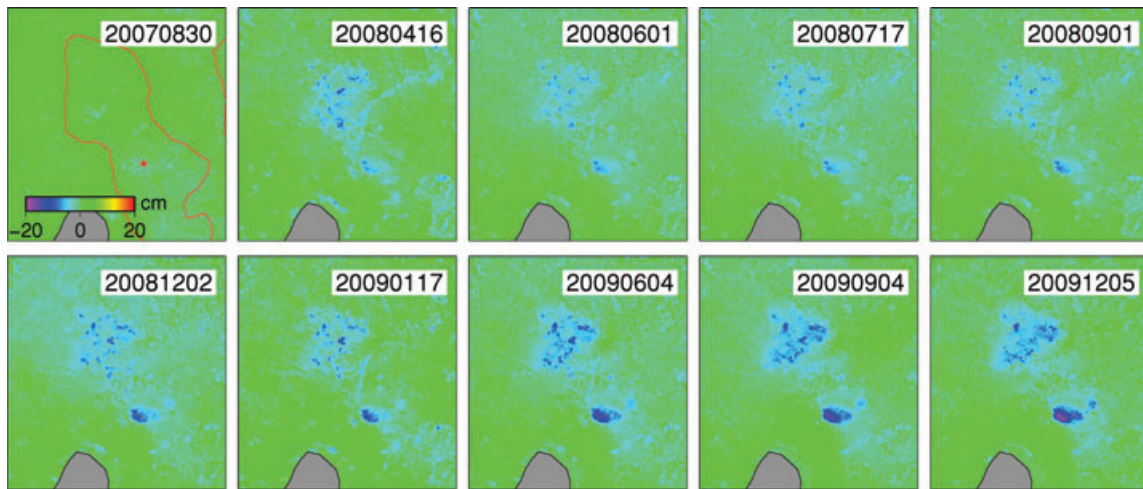**Figure 8.** Time series of line-of-sight displacement at Tauhara-Wairakei geothermal system from ALOS PALSAR descending path 628 starting from 20070715 (date in YYYYMMDD format). Coordinates of TL and BR corners are (−38.58N, 176.00E) and (−38.72N, 176.17E). Red star shows region of fastest subsidence.
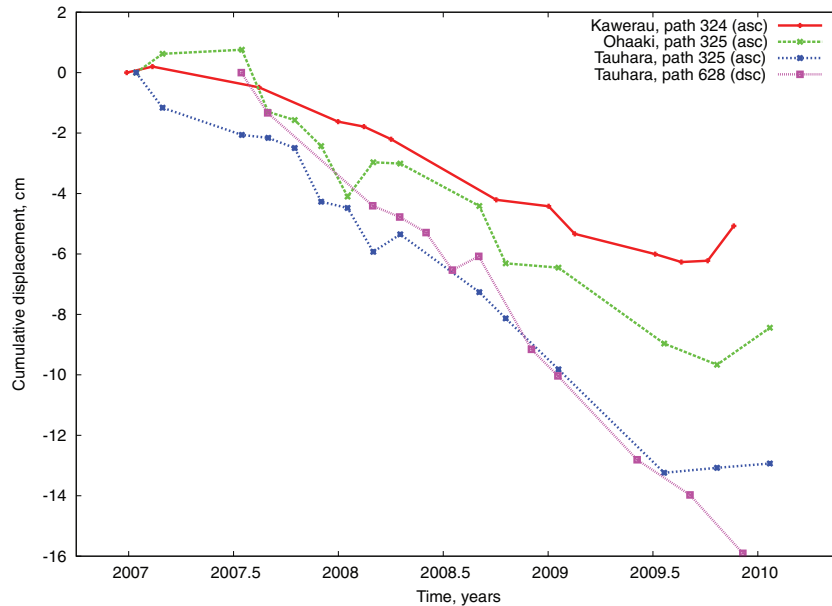

Figure 9. Time series of line-of-sight displacement for the 10×10 pixel region of fastest deformation rate at Kawerau, Ohaaki and Tauhara geothermal fields. These regions are labelled with red star in Figs 5–8.

reservoir can be approximated by an ellipsoidal shape. For these geothermal sites, we used data from the ascending and descending paths to solve for the best-fitting set of model parameters of a finite ellipsoidal pressure source (a prolate spheroid). For the Kawerau and Ohaaki regions we used data from ascending paths 324 and 325, respectively and for the Tauhara region we simultaneously used ascending and descending data from paths 325 and 628. We inverted the ALOS PALSAR displacement rates for the location (longitude, latitude and depth), orientation (strike and plunge angles) and volume change (ΔV) within the prolate spheroidal source. Originally, Yang *et al.* (1988) proposed expressions that fully characterize the spheroidal geometric dimensions (semi-axes and ΔP), but such parameters are normally poorly resolved. Therefore, we present our results as a single parameter, the volume change (ΔV), according to (Tiampo *et al.* 2000).

6.2 Tabular sources

For the Wairakei geothermal site we simultaneously used data from ascending and descending paths 325 and 628. In this region an electrical resistivity boundary marks the external limit of the high-pressure, high-temperature, fluid-rich region (Allis *et al.* 2009). Multiple production wells indicate that the reservoir lies at a depth of around 0.5–1.5 km, related to the Waiora 1 ignimbrite formation (Allis *et al.* 2009). Due to the shape of the observed deformation signal we assumed a tabular model (Okada 1985) to be more appropriate than an ellipsoidal one.

The stratigraphic formation acts as a confined aquifer, so we simulated the ground deformation with the spatially variable opening or closing of a horizontal rectangular tensile dislocation (Okada 1985), so the volume change in the tabular permeable formation can be simply deduced as, $\Delta V = sLW$ where, s is the opening/closure,
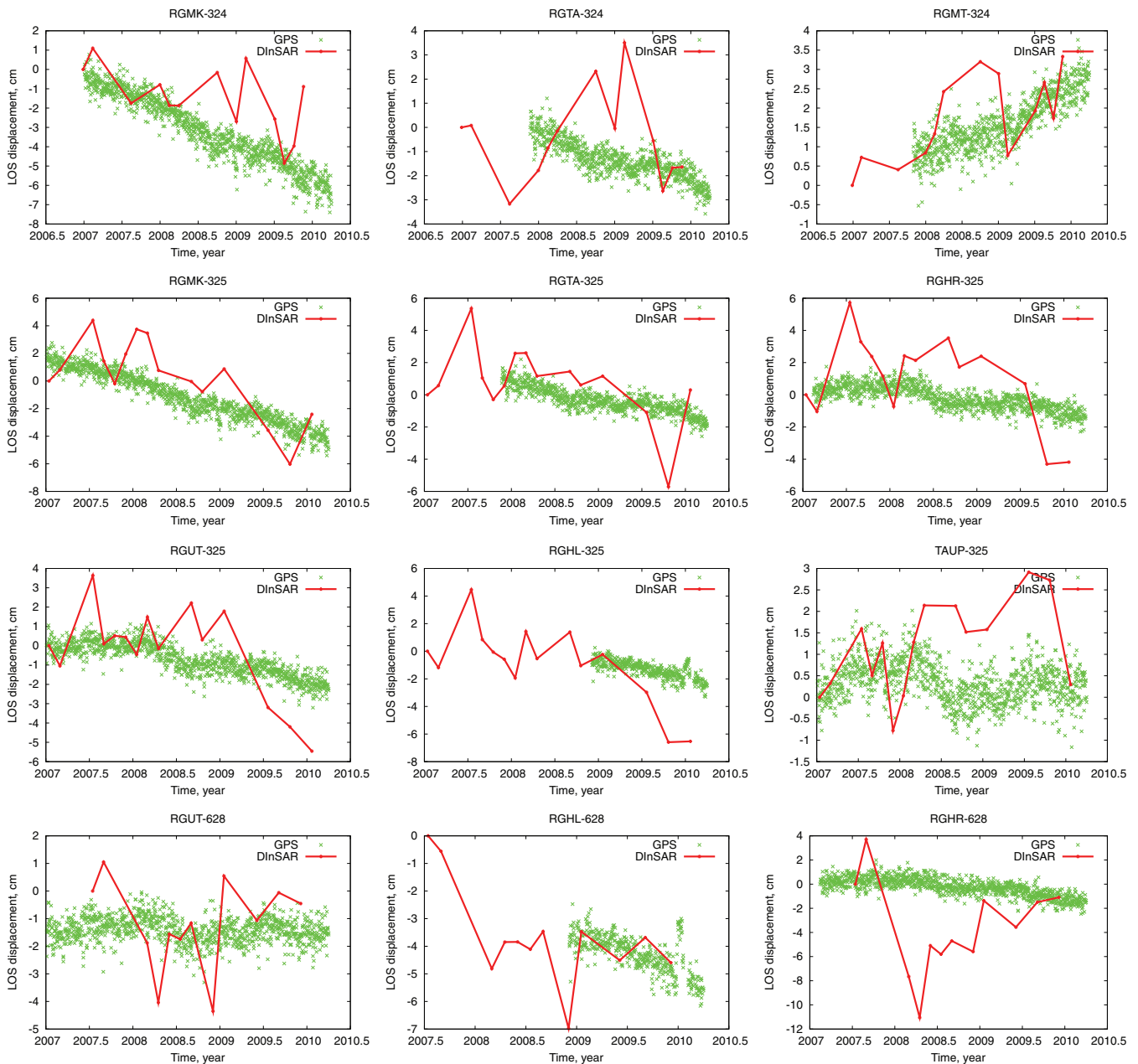
Figure 10. Time series of ground displacement in LOS geometry for some GPS sites.

L is the length of the dislocation and W its width. For simplicity, we assume that the tabular formation is horizontal and is located at 0.5 km depth. To allow for variable pressure change, the 10×10 km dislocation was divided into 40×40 smaller dislocations of 250 m side. We imposed a regularization factor that controls the smoothness of the volume change distribution ($\lambda^2 \nabla^2$), where λ is a penalty factor that weights the smoothness constraint, ∇^2 (the finite difference approximation of the Laplacian operator). The specific value of the parameter λ is somewhat subjective, and can be determined using an L-curve method (e.g. Gonzalez *et al.* 2010); for this case we choose $\lambda = 3$. A detailed discussion of the inversion procedure can be found in (Gonzalez *et al.* 2010; Samsonov *et al.* 2010).

6.3 Inversion results

Model parameters were determined using a simulated annealing (SA) global optimization algorithm. Such global optimization methods can be trapped into local minima (wrong solutions) (e.g. Shirzaei & Walter 2009). For that reason, we repeated the parameter search n times, where n is large enough to ensure a good exploration of the model parameters (in this case $n = 100$). The best-fitting model parameters are then estimated as median values of the n best-fitting individual solutions and standard deviations give an estimate of the parameter precision (Gonzalez *et al.* 2010). We also modified our method to provide more accurate error bounds as suggested in Efron & Tibshirani (1998).
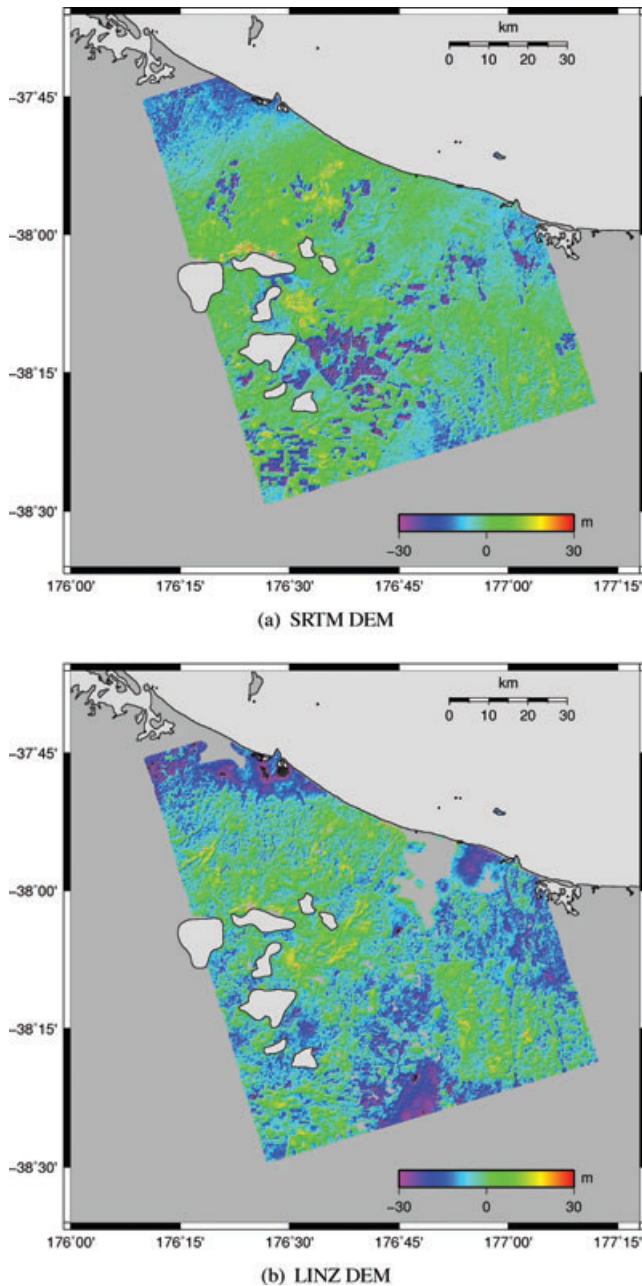
(a) SRTM DEM

(b) LINZ DEM

Figure 11. Topographic corrections for two digital elevation models (SRTM and LINZ) calculated using modified SBAS technique (Samsonov 2010; Samsonov *et al.* 2011).

In Table 2, we present the best-fitting model parameters for the studied geothermal sites. The ellipsoidal source results for Kawerau, Ohaaki and Tauhara are presented in Fig. 13. Kawerau geothermal field can be represented by a single ellipsoidal source located at a depth of 1.3 km with volume change -0.13×10^6 m^3 yr^{-1}. Subsidence at Ohaaki can be modelled by a single ellipsoidal source located at a depth of 1.5 km with volume change -0.27×10^6 m^3 yr^{-1}. For Tauhara geothermal field our model determined a source at 0.4 km depth with a volume change of -0.07×10^6 m^3 yr^{-1}. We assumed a 0.5 km depth for the tabular source beneath Wairakei and its estimated shape and volume change equal to -47.1×10^6 m^3 yr^{-1}.

We wished to compare our modelled volume change rates with measured rates, but these rates are not available to us as they are considered commercially sensitive by the power companies. We
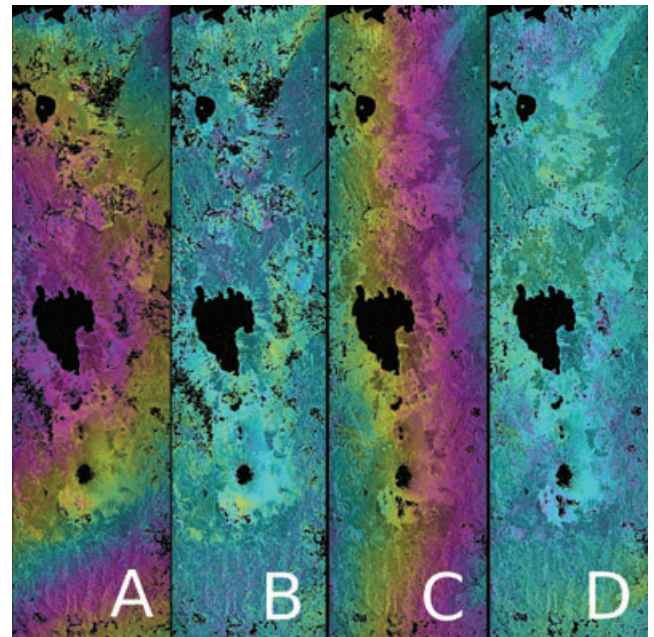

Figure 12. Example of two unwrapped interferograms (path 628) before and after orbital correction applied. Interferograms 20080717-20081202 (A) and 20090604-20091205 (C) displays quadratic and linear trends correspondingly. These signals were successfully removed, corrected interferograms are shown in (B) and (D). Complete colour cycle corresponds to about 12 cm of apparent line-of-sight deformation.

calculated an approximate total extraction rate for Wairakei of $\Delta V \sim -40 \times 10^6$ m^3 yr^{-1}) from extraction and reinjection rates provided in (Bixley *et al.* 2009) and the results are similar to those above (i.e. $\Delta V = -47.1 \times 10^6$ m^3 yr^{-1}). At the same time, we have to be careful comparing these rates since our calculated rates are the sum of extraction rates and natural and artificial recharge rates, and the natural recharge rates are not known.

7 CONCLUSIONS

We performed processing of the ALOS PALSAR Synthetic Aperture Radar images from two ascending paths and one descending path over the TVZ, New Zealand. We utilized an improved version of the Small Baseline Subset algorithm to produce linear LOS ground displacement rates and their uncertainties, and time series of deformation for each path. The 1σ uncertainties in the DInSAR displacement rates vary from 0.5 to 0.8 cm yr^{-1} on two ascending paths, but are up to 2 cm yr^{-1} on the descending path. We compared the DInSAR displacement rates with cGPS velocities and found good agreement between cGPS and DInSAR for the two ascending paths. The DInSAR uncertainties were too large to make a useful comparison on the third path.

Localized subsidence was observed at Kawerau, Ohaaki and Tauhara-Wairakei geothermal regions. For each geothermal region, we calculated time series of deformation and modelled the displacement rates using simplified ellipsoidal or tabular sources. We inverted for source location, volume rate of change, and in some cases depth. In the one case where ground truth data on volume change rates could be estimated, we found these to be in reasonable agreement with the DInSAR estimates.

Based on our work we conclude that the precision of L-band ALOS PALSAR is sufficient for identifying localized regions of ground deformation with amplitudes over a few centimetre per year

Table 2. Best-fitting parameters of ellipsoidal sources for Kawerau, Ohaaki and Tauhara geothermal fields.

	Kawerau	Ohaaki	Tauhara	Wairakei
Longitude (° ±km)	176.698 ± 0.20	176.306 ± 0.43	176.084 ± 0.13	176.08
Latitude, (° ±km)	-38.055 ± 0.15	-38.524 ± 0.19	-38.676 ± 0.09	-38.62
Depth (km)	1.3 ± 0.2	1.5 ± 0.3	0.4 ± 0.2	0.5^c
ΔV^a, $\times 10^6$ m^3	-0.13 ± 0.05	-0.27 ± 0.09	-0.07 ± 0.03	-47.1
Strike (°)	60 ± 84	125 ± 103	$-63^b \pm 18$	
Dip (°)	32 ± 25	28 ± 25	0^c	
ϵ	0.24	0.78	0.89	
RMS	0.2	0.2	0.3	

^{a}Parameter determined as $\Delta V = \frac{\Delta P}{\mu} \pi a b^2$ (Tiampo *et al.* 2000).
^{b}Constrained to the range $[-75, -30]$ (positive degrees N-to-E, clockwise).
^{c}Fixed during the inversion. ϵ is eccentricity parameter.

(a) Kawerau   (b) residual   (c) Ohaaki   (d) residual

(e) Tauhara-Wairakei (asc)   (f) residual (asc)   (g) Tauhara-Wairakei (dsc)   (h) residual (dsc)
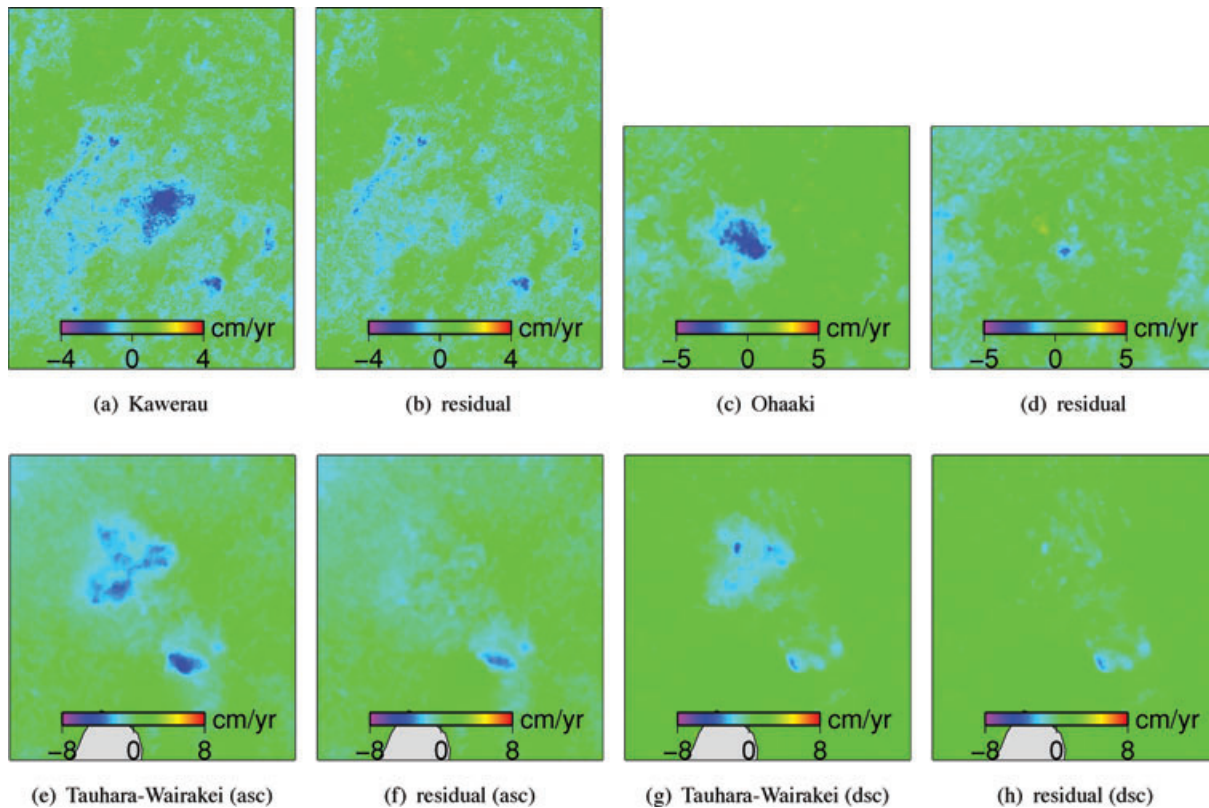
Figure 13. Results of modelling with ellipsoidal sources (Yang *et al.* 1988) and tabular source (Okada 1985). Top row—observed (a) and residual (b) linear displacement rates for Kawerau [coordinates of TL and BR corners are (−37.95N, 176.60E) and (−38.15N, 176.80E)] and Ohaaki [observed (c) and residual (d), coordinates of TL and BR corners are (−38.48N, 176.25E) and (−38.58N, 176.40E)]. Bottom row—results of modelling with tabular source (Okada, 1985) for Wairakei and ellipsoidal (Yang *et al.* 1988) source for Tauhara (coordinates of TL and BR corners are (−38.58N, 176.00E) and (−38.72N, 176.17E)). Observed (e) and (g) and residual (f) and (h) linear displacement rates for Tauhara-Wairakei geothermal system from ascending and descending orbits.

when sufficient number of images are available for time-series analysis. To estimate the deformation rate of such signals it is necessary to properly estimate residual topographic phase, which can be done, for example, by using code presented in (Samsonov *et al.* 2011). The topographic correction is recommended even for high-accuracy high-resolution DEMs acquired by other means than L-band SAR due to dependence of the penetration depth on sensor wavelength. This effect is particularly clearly observed in our residual topographic results calculated using the 90 m SRTM DEM (e.g. agricultural fields at the bottom of Fig. 11).

The linear and quadratic trends caused by inaccurate orbital estimation and long wavelength ionospheric noise are present in many interferograms, and need to be corrected before moving to the advanced processing steps. From a practical point of view such signals are easy to remove by fitting a linear or quadratic surface or by performing orbit refinement. However, such algorithms also remove long wavelength deformation signals. Therefore, low magnitude long wavelength tectonic signals are impossible to measure directly until the accuracy of the orbital information is improved. It seems feasible that methods could be developed based on prior knowledge of the tectonic deformation; however, such techniques have not been tested in this work.

We also found that the precision of SBAS analysis decreases proportionally to the size of the interferogram. We observed the

best correlation between GPS and DInSAR for interferograms consisting of only one frame, and the worst correlation for interferograms consisting of four frames. The decrease of precision is caused by higher degree (than quadratic) variations in atmospheric and residual orbital components mixed together. It is anticipated that high-resolution ionospheric models can be derived from GPS measurements in regions with good GPS coverage and used in interferometric processing before or during SBAS analysis.

The generally good agreement between the rates of LOS displacement measured by DInSAR and cGPS and the good coherence of L-band interferograms is encouraging for the application of L-band DInSAR in other regions with significant vegetation cover.

REFERENCES

Allis, R., 2000. Review of subsidence at Wairakei field, New Zealand, *Geothermics, 29*(4–5), 455–478.

Allis, R., Bromley, C. & Currie, S., 2009. 2009 Update on subsidence at the Wairakei-Tauhara geothermal system, New Zealand, *Geothermics, 38*(1), 169–180.

Beavan, J., 2005. Noise properties of continuous GPS data from concrete-pillar geodetic monuments in New Zealand, and comparison with data from U.S. deep drilled braced monuments *J. geophys. Res., 110*(B8), B08410, doi:10.1029/2005JB003642.

Beavan, J. & Haines, J., 2001. Contemporary horizontal velocity and strain-rate fields of the Pacific-Australian plate boundary zone through New Zealand, *J. geophys. Res., 106*(B1), 741–770.

Beavan, J., Tregoning, P., Bevis, M., Kato, T. & Meertens, C., 2002. The motion and rigidity of the Pacific Plate and implications for plate boundary deformation, *J. geophys. Res., 107*(B10), 2261, doi:10.1029/2001JB000282.

Berardino, P., Fornaro, G. & Lanari, R., 2002. A new algorithm for surface deformation monitoring based on small baseline differential SAR interferograms, *IEEE Trans. Geosci. Remote Sens., 40*(11), 2375–2383.

Bibby, H., Caldwell, T., Davey, F. & Webb, T., 1995. Geophysical evidence on the structure of the Taupo Volcanic Zone and its hydrothermal circulation, *J. Volc. Geotherm. Res., 68*, 29–58.

Bixley, P., Clotworthy, A. & Mannington, W., 2009. Evolution of the Wairakei geothermal reservoir during 50 years of production, *Geothermics, 38*(1), 145–154.

Bromley, C., Currie, S., Manville, V. & Rosenberg, M., 2009. Recent ground deformation subsidence at Crown Road, Tauhara and its probable causes, *Geothermics, 38*, 181–191.

Burgmann, R., Hilley, G., Ferretti, A. & Novali, F., 2006. Resolving vertical tectonics in the San Francisco Bay Area from permanent scatterer InSAR and GPS analysis, *Geology, 34*(3), 221–224.

Dach, R., Hugentobler, U., Fridez, P. & Meindl, M., 2007. *Bernese GPS Software Version 5.0,* Astronomical Institute, University of Bern.

Darby, D., Hodgkinson, K. & Blick, G., 2000. Geodetic measurement of deformation in the Taupo Volcanic Zone, New Zealand: the North Taupo network revisited, *New Zealand J. Geol. Geophys., 43*(2), 157–170.

Efron, B. & Tibshirani, R., 1998. The problem of regions, *Ann. Stat., 26,* 1687–1718.

Ferretti, A., Prati, C. & Rocca, F., 2000. Nonlinear subsidence rate estimation using permanent scatterers in differential SAR interferometry, *IEEE Trans. Geosci. Remote Sens., 38*(5), 2202–2212.

Gonzalez, P., Tiampo, K., Camacho, A. & Fernandez, J., 2010. Shallow flank deformation at Cumbre Vieja volcano (Canary Islands): implications on the stability of steep-sided volcano flanks at oceanic islands, *Earth planet. Sci. Lett., 297*, 545–557, doi:10.1016/j.epsl.2010.07.006

Hole, J., Bromley, C., Stevens, N. & Wadge, G., 2007. Subsidence in the geothermal fields of the Taupo Volcanic Zone, New Zealand from 1996 to 2005 measured by InSAR, *J. Volc. Geother. Res., 166*(3-4), 125–146.

Hooper, A., Segall, P., Johnson, K. & Rubinstein, J., 2002. Reconciling seismic and geodetic models of the 1989 Kilauea south flank earthquake, *Geophys. Res. Lett., 29,* doi:10.1029/2002GL016156.

Houghton, B., Wilson, C., McWilliams, M., Lanphere, M., Weaver, C., Briggs, R. & Pringle, M., 1995. Chronology and dynamics of a large silicic magmatic system: Central Taupo Volcanic Zone, New Zealand, *Geology, 23*(1), 13–16.

Kwoun, O., Lu, Z., Neal, C. & Wicks, C., 2006. Quiescent deformation of the Aniakchak Caldera, Alaska, mapped by InSAR, *Geology, 34*(1), 5–8.

Lanari, R., Lundgren, P., Manzo, M. & Casu, F., 2004a. Satellite radar interferometry time series analysis of surface deformations for Los Angeles, California, *Geophys. Res. Lett., 31,* doi:10.1029/2004GL021294.

Lanari, R., Mora, O., Manunta, M., Mallorqui, J., Berardino, P. & Sansosti, E., 2004b. A small-baseline approach for investigating deformations on full-resolution differential SAR interferograms, *IEEE Trans. Geosci. Remote Sens., 42*(7), 1377–1386.

Manconi, A., Walter, T. & Amelung, F., 2007. Effects of mechanical layering on volcano deformation, *Geophys. J. Int., 170,* 952–958, doi:10.1111/j.1365-246X.2007.03449.x.

Massonnet, D. & Feigl, K., 1998. Radar interferometry and its application to changes in the Earth surface, *Rev. Geophys., 36*(4), 441–500.

Meyer, F., Bamler, R., Jakowski, N. & Fritz, T., 2006. The potential of low-frequency SAR systems for mapping ionospheric TEC distributions, *IEEE Geosci. Remote Sens. Lett., 3*(4), 560–564.

Niell, A., 1996. Global mapping functions for the atmosphere delay at radio wavelength, *J. geophys. Res., 101*(B2), 3227–3246.

Okada, Y., 1985. Surface deformation due to shear and tensile faults in a half-space, *Bull. seism. Soc. Am., 75*(4), 1135–1154.

Peltier, A., Hurst, T., Scott, B. & Cayol, V., 2009. Structures involved in the vertical deformation at Lake Taupo (New Zealand) between 1979 and 2007: new insights from numerical modelling, *J. Volc. Geother. Res., 181,* 173–184.

Press, W., Teukolsky, S., Vetterling, W. & Flannery, B., 2007. *Numerical Recipes in C: The Art of Scientific Computing,* 3rd edn, 994pp., Cambridge University Press, Cambridge.

Rignot, E., 2000. Effect of Faraday Rotation on L-band interferometric and polarimetric synthetic-aperture radar data, *IEEE Trans. Geosci. Remote Sens., 38*(1), 383–390.

Rosen, P., Hensley, P., Joughin, I., Li, F., Madsen, S., Rodriguez, E. & Goldstein, R., 2000. Synthetic aperture radar interferometry, *Proc. IEEE, 88*(3), 333–382.

Rosenqvist, A., Shimada, M., Ito, N. & Watanabe, M., 2007. ALOS PALSAR: a pathfinder mission for global-scale monitoring of the environment, *IEEE Trans. Geosci. Remote Sens., 45*(11), 3307–3316.

Samsonov, S., 2010. Topographic correction for ALOS PALSAR interferometry, *IEEE Trans. Geosci. Remote Sens.,* **48**(7), 3020–3027.

Samsonov, S., Beavan, J., Bromley, C., Scott, B., Jolly, G. & Tiampo, K., 2008. ALOS PALSAR interferometry of Taupo Volcanic Zone, New Zealand, in *Proceedings of the ALOS PI 2008 Symposium,* 2008 November 3–7, Rhodes, Greece, ESA SP-466, eds Lacoste, H. & Ouwehand, L., ESA Publications Division, Noordwijk.

Samsonov, S., Tiampo, K., Gonzalez, P., Manville, V. & Jolly, G., 2010. Modelling deformation occurring in the city of Auckland, New Zealand mapped by the Differential Synthetic Aperture Radar, *J. geophys. Res.,* **115**, B08410, doi:10.1029/2009JB006806.

Samsonov, S., van der Koij, M. & Tiampo, K., 2011. A simultaneous inversion for deformation rates and topographic errors of DInSAR data utilizing linear least square inversion technique, *Comput. Geosci.,* in press, doi:10.1016/j.cageo.2011.01.007.

Sandwell, D. & Price, E., 1998. Phase gradient approach to stacking interferograms, *J. geophys. Res.,* **103**(B12), 30 183–30 204.

Shirzaei, M. & Walter, T., 2009. Randomly iterated search and statistical competency as powerful inversion tools for deformation source modeling: application to volcano interferometric synthetic aperture radar data, *J. geophys. Res.,* **114**, B10401, doi:10.1029/2008JB006071.

Stagpoole, V. & Bibby, H., 1998. The shallow-resistivity structure of the Taupo Volcanic Zone, New Zealand, in *Proceedings of the 20th N. Z. Geothermal Workshop University of Auckland,* Auckland, pp. 303–310.

Stratford, W. & Stern, T., 2004. Strong seismic reflections and melts in the mantle of a continental back-arc basin, *Geophys. Res. Lett.,* **31**, L0622, doi:10.1029/2003GL019232.

Tiampo, K., Rundle, J., Fernandez, J. & Langbein, J., 2000. Spherical and ellipsoidal volcanic sources at Long Valley caldera, California, using a genetic algorithm inversion technique, *J. Volc. Geotherm. Res.,* **102**(3-4), 189–206.

Usai, S., 2003. A least squares database approach for sar interferometric data, *IEEE Trans. Geosci. Remote Sens.,* **41**(4), 753–760.

Villamor, P. & Berryman, K., 2001. A late Quaternary extension rate in the Taupo Volcanic Zone, New Zealand, derived from fault slip data, *New Zealand J. Geol. Geophys.,* **44**, 243–269.

Wallace, L., Beavan, J., McCaffrey, R. & Darby, D., 2004. Subduction zone coupling and tectonic block rotations in the North Island New Zealand, *J. geophys. Res.,* **109**, B12406, doi:10.1029/2004JB003241.

Wdowinski, S., Bock, Y., Zhang, J., Fang, P. & Genrich, J., 1997. Southern California Permanent GPS Geodetic Array: spatial filtering of daily positions for estimating coseismic and postseismic displacements induced by the 1992 Landers earthquake, *J. geophys. Res.,* **102**, 18 057–18 070.

Wegmuller, U. & Werner, C., 1997. Gamma SAR processor and interferometry software, in *Third ERS Symposium on Space at the service of our Environment,* Florence, Italy.

Wilson, C., Houghton, B., McWilliams, M., Lanphere, M., Weaver, S. & Briggs, R., 1995. Volcanic and structural evolution of the Taupo Volcanic Zone, New Zealand: a review, *J. Volc. Geotherm. Res.,* **68**(1-3), 1–28.

Yang, X., Davis, P. & Dieterich, J., 1988. Deformation from inflation of a dipping finite prolate spheroid in an elastic half-space as a model for volcanic stressing, *J. geophys. Res.,* **76**(B5), 4257–4289.

SUPPORTING INFORMATION

Additional Supporting Information may be found in the online version of this article:

Supplement. This electronic supplement provides figures that are referenced in the main text and may be beneficial for the overall understanding of the results presented in the main text.

Please note: Wiley-Blackwell are not responsible for the content or functionality of any supporting materials supplied by the authors. Any queries (other than missing material) should be directed to the corresponding author for the article.